TEST EVOLUTION OF NON-AXISYMMETRIC GRAVITATIONAL WAVES

Leonardo Sigalotti [1] and Richard F. Stark [2] *
[1] International Center for Theoretical Physics,
Strada Costiera 11, 34100 Trieste, Italy
[2] University of Ljubljana, Department of Physics,
Jadranska 19, 61000 Ljubljana, Slovenia

Abstract: We give a preliminary report on one of the tests we have performed of a full non-axisymmetric general relativistic code. The test considered here concerns the numerical evolution of vacuum non-axisymmetric gravitational waves and their comparison at low amplitudes with theoretical waveforms obtained from linearised theory.

PACS numbers: 04.25.Dm, 04.30.-w, 04.20.-q

I. Introduction

We are currently carrying out a number of detailed tests of a full non-axisymmetric general relativistic code which solves the coupled Einstein and hydrodynamic equations using the '3+1' ADM formalism in the radial gauge with mixed slicing [1]. The code has been written in particular to obtain directly the gravitational wave emission from non-axisymmetric rotating gravitational collapse. The test we report here concerns the numerical evolution of vacuum non-axisymmetric gravitational waves and their comparison at low amplitudes with theoretical waveforms obtained using linearised theory. This report should be considered preliminary, since the code is still under active development.

We consider the propagation of non-axisymmetric $l = 2$ and $l = 4$, and different m, linearised gravitational waves. We are able to use essentially analytic predictions for these waves with which to compare to the numerical solutions. To obtain these, we take an even mode linearised axisymmetric solutions for a given $l = l_w$, and rotate this by $\pi/2$

* E-mail address: richard@fiz.uni-lj.si *and* norver@stark1.freeserve.co.uk

so that the symmetry axis now lies in the equator. This generates a non-axisymmetric solution which is a linear combination of all l up to l_w and all even m. (This solution also satisfies the symmetry and regularity conditions we have assumed). Under this rotation, both even and odd waves are generated. The solution is determined by an arbitrary wave amplitude $F(t-r)$ or $F(t+r)$ for the retarded or advanced solutions respectively. Although each solution is by itself singular at the origin, the combination of (advanced − retarded) solution is non-singular everywhere. We choose a particular function F; construct initial data at $t = 0$; and evolve this initial data and observe the outgoing waveform leaving the outer grid radius. We then compare this with the analytic solution.

II. Radial gauge and mixed slicing

We will not list here the full non-axisymmetric '3+1' equations for our gauge choice. These can be found in ref.[2] and will be more fully discussed in a forthcoming paper [1]. We give here only the briefest details in order to define the variables used in our wave solution.

We use spherical spatial coordinates (r,θ,ϕ). The spatial metric h_{ij} $(i, j = 1, 2, 3)$ in the radial gauge [1-4] is determined from the conditions that the off-diagonal (r,θ) (r,ϕ) components of the metric be zero, and that the angular spatial determinant be fixed to its Euclidean value. Thus we have:

$$h_{r\theta} = 0, \tag{1a}$$

$$h_{r\phi} = 0, \tag{1b}$$

$$(h_{\theta\theta}h_{\phi\phi} - h_{\theta\phi}^2) = r^4 \sin^2\theta. \tag{1c}$$

The 3-dimensional metric is then determined by the three functions A, η, and ξ, each functions of (t, r, θ, ϕ), and the full 4-dimensional metric has the form:

$$ds^2 = -(N^2 - N^iN_i)dt^2 - 2N_idx^idt + A^2dr^2 + r^2B^{-2}d\theta^2 + r^2B^2(\sin\theta d\phi + \xi d\theta)^2, \tag{2}$$

with $B^2 = 1 + \eta$, and where η and ξ are respectively the even and odd dynamical degrees of freedom in the sense that they tend (for this linearised test, and within a sign) at large radii to the even and odd transverse traceless amplitudes h_+,$h_\times$. N is the lapse; N^i the shift vector raised and lowered using h_{ij}.

The components of the extrinsic curvature we use are based on the orthonormal components $K_{(i)(j)}$ $(i, j = 1, 2, 3)$ which are the components of K_{ij} projected onto the orthonormal triad of basis vectors:

$$e^i_{(1)} = [A^{-1}, 0, 0]; \quad e^i_{(2)} = [0, B/r, -\xi B/(r\sin\theta)]; \quad e^i_{(3)} = [0, 0, 1/(Br\sin\theta)]. \tag{3}$$

The computed geometrical variables are (we do not discuss here the accompanying hydrodynamic variables):

$$\text{Spatial metric}: \qquad A; \qquad \eta; \qquad \xi; \tag{4a}$$

Extrinsic curvature: $\qquad K_1 = K_{(1)(1)}; \qquad K_2 = BK_{(1)(2)}/\sin\theta;$

$$K_3 = BK_{(1)(3)}/\sin\theta; \qquad K_+ = \frac{1}{2}B^2(K_{(3)(3)} - K_{(2)(2)}); \qquad K_\times = B^2K_{(2)(3)}; \tag{4b}$$

$$\text{Lapse and shift}: \qquad N; \qquad \beta^r = N^r/r; \qquad G = N^\theta/\sin\theta; \qquad N^\phi. \tag{4c}$$

.

Following ref.[4] we use a mixed foliation condition consisting of a linear combination (depending on radius) of polar and maximal slicing: we set

$$\text{trace}(K_i{}^j) = (1 - C(r))K_r{}^r, \tag{5}$$

where $0 \leq C(r) \leq 1$ is a chosen smooth function of radius such that $C(0) = 1$ and $C(r > r_0) = 0$ (corresponding to maximal slicing at the origin and polar slicing for radii larger than a chosen transition radius r_0). The actual form of $C(r)$ used is:

$$C(r) = [1 - (r/r_0)^2]^n, \tag{6}$$

with $r_0 = r_0(t)$, n chosen values.

Regularity at the origin is determined by requiring the components in the 'cartesian' $(\hat{x},\hat{y},\hat{z})$ system of coordinates be expandable in non-negative integer powers of $(\hat{x},\hat{y},\hat{z})$ (consistent with the symmetry assumed) [4]. $(\hat{x},\hat{y},\hat{z}$ are quasi-cartesian coordinates related to r,θ,ϕ in the usual manner). This gives, in the linearised case (with no mean origin azimuthal shift rotation), the following values for the origin shift and extrinsic curvature:

$$\beta^r(r=0) = \{k_+(3\cos^2\theta - 1) + (k_-\cos 2\phi - k_\times \sin 2\phi)\sin^2\theta\}, \tag{7a}$$

$$G(r=0) = \{-3k_+ - k_\times \sin 2\phi + k_-\cos 2\phi\}\cos\theta, \tag{7b}$$

$$N^\phi(r=0) = \{-k_-\sin 2\phi - k_\times \cos 2\phi\}, \tag{7c}$$

$$K_+(r=0) = \frac{3}{2}k_+\sin^2\theta + \frac{1}{2}(1+\cos^2\theta)[-k_\times \sin 2\phi + k_-\cos 2\phi], \tag{8a}$$

$$K_\times(r=0) = \cos\theta[k_-\sin 2\phi + k_\times \cos 2\phi], \tag{8b}$$

$$K_1(r=0) = k_+(1 - 3\cos^2\theta) + \sin^2\theta[-k_-\cos 2\phi + k_\times \sin 2\phi], \tag{8c}$$

$$K_2(r=0) = \cos\theta[3k_+ - k_-\cos 2\phi + k_\times \sin 2\phi], \tag{8d}$$

$$K_3(r=0) = [k_-\sin 2\phi + k_\times \cos 2\phi]. \tag{8e}$$

where $k_+(t)$, $k_-(t)$, $k_\times(t)$ are time dependent coefficients.

Also we have near the origin:

$$\eta = O(r^2), \tag{9}$$

$$N = N(r=0) + O(r^2). \tag{10}$$

III. Axisymmetric linearised gravitational waves

The axisymmetric solution we rotate is based on one found by Bardeen [5,6] (see also ref.[7] where axisymmetric comparison tests are also shown). Bardeen's solution corresponds to a general l even mode Teukolsky wave [8] transformed from the transverse-traceless gauge to the radial gauge with maximal slicing. For completeness, we have generalised Bardeen's solution (which is for maximal slicing) to the case of mixed slicing by obtaining the linearised axisymmetric equations in the radial gauge with mixed slicing. As we explain below however, the original Bardeen solution is actually sufficient, even for mixed slicing, for the comparison with the computed outgoing waves.

Following Bardeen [5,6], we write the even linearised solution for each $l \geq 2$ in the form:

$$(A-1) = \alpha_l P_{l0}, \tag{11a}$$

$$\eta = [c_l + \frac{(a_l - 2f_l)}{l(l+1)}](1-x^2)P_{l0,xx}\,, \tag{11b}$$

$$\xi = 0, \tag{11c}$$

$$K_1 = -\dot{a}_l P_{l0}, \tag{11d}$$

$$K_2 = -\frac{1}{2}\dot{b}_l P_{l0,x}\,, \tag{11e}$$

$$K_3 = 0, \tag{11f}$$

$$K_+ = -\frac{1}{2}\dot{c}_l(1-x^2)P_{l0,xx}\,, \tag{11g}$$

$$K_\times = 0, \tag{11h}$$

$$G = \frac{(2\dot{f}_l - \dot{a}_l)}{l(l+1)}P_{l0,x}\,, \tag{11i}$$

$$N^\phi = 0, \tag{11j}$$

$$\beta^r = [-\dot{f}_l + \frac{1}{2}\dot{a}_l(1-C(r))]P_{l0}, \tag{11k}$$

$$N = n_l P_{l0}, \tag{11l}$$

where $\dot{} \equiv (\frac{\partial}{\partial t})_r$. In this form, the evolution equation for η [1,2] is automatically satisfied. The equation for β^r [1,2] is also satisfied.

The momentum constraints for K_1 and K_2 [1,2] require:

$$b_l = -\frac{2}{l(l+1)}\{r^{-2}[r^3 a_l]_{,r} - [r(1-C(r))a_l]_{,r}\}, \tag{12}$$

$$c_l = \frac{1}{(l-1)(l+2)}\{r^{-2}[r^3 b_l]_{,r} + a_l + (1-C(r))a_l\}. \tag{13}$$

The shift equation for G [1,2] provides an ordinary differential equation for f_l:

$$2r f_{l,r} + l(l+1) f_l = -r a_{l,r} - 6a_l + 2[r(1-C(r))a_l]_{,r} + \frac{1}{2} l(l+1)(1-C(r))a_l. \tag{14}$$

The origin boundary conditions (7),(8) (in the axisymmetric limit) and (9), give for the origin boundary condition for f_l:

$$f_l(r=0) = \begin{cases} -a_l(r=0), & \text{for } l=2; \\ 0, & \text{for } l>2 \end{cases}. \tag{15}$$

The evolution equation for A [1,2] gives:

$$\alpha_l = a_l + f_l + r f_{l,r} - \frac{1}{2}[(1-C(r))r a_l]_{,r}\,, \tag{16}$$

or equivalently using (14) for f_l:

$$\alpha_l = -2a_l - \frac{1}{2} r a_{l,r} - \frac{1}{2}(l-1)(l+2) f_l + \frac{1}{2}[(1-C(r))r a_l]_{,r} + \frac{1}{4} l(l+1)(1-C(r))a_l. \tag{17}$$

The evolution equation for K_1 [1,2] gives (using (16),(17)):

$$r^2 \ddot{a}_l = r^2 n_{l,rr} + r^2 a_{l,rr} + 6r a_{l,r} - (l+3)(l-2)a_l - [r^2(1-C(r))a_l]_{,rr}\,, \tag{18}$$

while the lapse equation [1,2], using (18), gives:

$$r^2 n_{l,rr} + 2r n_{l,r} - l(l+1) n_l = (1-C(r)) r^2 \ddot{a}_l, \tag{19}$$

with origin boundary conditions (10):

$$n_l(r=0) = 0;\ n_{l,r}(r=0) = 0. \tag{20}$$

The remaining equations: the Hamiltonian constraint [1,2], and the K_2 evolution equation [1,2], are then also satisfied by these solutions.

For the case of maximal slicing ($C(r) = 1$) we can explicitly solve (18),(19) for a_l, n_l and recover Bardeen's solution. In this case, the solution for n_l is simply:

$$n_l = 0. \tag{21}$$

The solution for a_l for the case of a retarded solution (where t occurs only in the form of retarded time $(t - r)$) is found using the form:

$$a_l = \sum_n c_n r^{-(n+3)} F_l^{(l-n)}(t - r), \tag{22}$$

where $F_l^{(k)}$ indicates the k'th derivative with respect to the arbitrary generating function F_l for the l'th mode. Substitution into (18) gives for the coefficients c_n:

$$c_n = c_{n-1} \frac{(l + n)(l - n + 1)}{2n}, \tag{23}$$

leading to the retarded solution:

$$a_l = \sum_{n=0}^{l} \frac{(l + n)!}{2^n n!(l - n)!} r^{-(n+3)} F_l^{(l-n)}(t - r). \tag{24}$$

The advanced solution is:

$$a_l = \sum_{n=0}^{l} \frac{(l + n)!}{2^n n!(l - n)!} (-1)^n r^{-(n+3)} F_l^{(l-n)}(t + r), \tag{25}$$

while the non-singular (advanced $-$ retarded) solution is:

$$a_l = \sum_{n=0}^{l} \frac{(l + n)!}{2^n n!(l - n)!} r^{-(n+3)} [(-1)^n F_l^{(l-n)}(t + r) - F_l^{(l-n)}(t - r)]. \tag{26}$$

Substituting the non-singular solution (26) for a_l into (14) (with $C(r) = 1$) we find for f_l:

$$f_l = \sum_{n=0}^{l} \frac{(l + n)!}{2^{n+1} n!(l - n)!} r^{-\frac{1}{2}l(l+1)} \int_0^r dr r^{[\frac{1}{2}l(l+1)-n-4]} \{$$

$$-r[(-1)^n F_l^{(l-n+1)}(t+r) + F_l^{(l-n+1)}(t-r)] + (n-3)[(-1)^n F_l^{(l-n)}(t+r) - F_l^{(l-n)}(t-r)]\}. \tag{27}$$

The integral can be evaluated either directly, or by reducing it using integration by parts to recurrence relations involving the $F_l^{(k)}(t \pm r)$.

The outgoing waveform at asymptotically large radii of the transverse traceless amplitudes is:

$$h_+ = -\frac{2}{(l-1)l(l+1)(l+2)} r^{-1} F^{(l+2)}(t-r)(1-x^2)P_{l0,xx} \quad (r\to\infty), \tag{28}$$

$$h_\times = 0. \tag{29}$$

IV. Generation of non-axisymmetric linearised gravitational waves

We now rotate this solution, with the symmetry axis of the wave rotated into the equator, to generate a non-axisymmetric solution. The relation between (θ,ϕ) to the rotated (θ',ϕ') coordinates aligned with the symmetry axis of the wave (which when rotated lies in the equator at an angle α to the $\hat{x}$ axis of the (θ,ϕ) system, corresponding to $\hat{x}' = -\hat{z}$; $\hat{y}' = \hat{y}\cos\alpha - \hat{x}\sin\alpha$; $\hat{z}' = \hat{x}\cos\alpha + \hat{y}\sin\alpha$; $r' = r$) is:

$$\sin\theta'\cos\phi' = -\cos\theta, \tag{30a}$$

$$\sin\theta'\sin\phi' = \sin\theta\sin(\phi-\alpha), \tag{30b}$$

$$\cos\theta' = \sin\theta\cos(\phi-\alpha). \tag{30c}$$

Under this rotation, to linear order, the geometrical variables become:

$$\eta(t,r,\theta,\phi) = \frac{\eta'(t,r,\theta')}{\sin^2\theta'}[\cos 2(\phi-\alpha) - \frac{1}{2}\sin^2\theta(1+\cos 2(\phi-\alpha))], \tag{31a}$$

$$\xi(t,r,\theta,\phi) = \frac{\eta'(t,r,\theta')}{\sin^2\theta'}\cos\theta\sin 2(\phi-\alpha), \tag{31b}$$

$$G(t,r,\theta,\phi) = -\frac{G'(t,r,\theta')}{\cos\theta'}\cos\theta\frac{1}{2}(1+\cos 2(\phi-\alpha)), \tag{31c}$$

$$N^\phi(t,r,\theta,\phi) = \frac{G'(t,r,\theta')}{\cos\theta'}\frac{1}{2}\sin 2(\phi-\alpha), \tag{31d}$$

$$\beta^r(t,r,\theta,\phi) = \beta^{r\prime}(t,r,\theta'), \tag{31e}$$

$$A(t,r,\theta,\phi) = A'(t,r,\theta'), \tag{31f}$$

$$N(t,r,\theta,\phi) = N'(t,r,\theta'), \tag{31g}$$

$$K_+(t,r,\theta,\phi) = \frac{K'_+(t,r,\theta')}{\sin^2\theta'}\frac{1}{2}[-\sin^2\theta + (1+\cos^2\theta)\cos 2(\phi-\alpha)], \tag{31h}$$

$$K_\times(t,r,\theta,\phi) = \frac{K'_+(t,r,\theta')}{\sin^2\theta'}\cos\theta\sin 2(\phi-\alpha), \tag{31i}$$

$$K_1(t,r,\theta,\phi) = K_1'(t,r,\theta'), \tag{31j}$$

$$K_2(t,r,\theta,\phi) = \frac{-K_2'(t,r,\theta')}{\cos\theta'}\frac{1}{2}\cos\theta(1+\cos 2(\phi-\alpha)), \tag{31k}$$

$$K_3(t,r,\theta,\phi) = \frac{K_2'(t,r,\theta')}{\cos\theta'}\frac{1}{2}\sin 2(\phi-\alpha). \tag{31l}$$

Applying these rotated values to the non-singular solution (26),(27) and expanding around the origin, we find the following values for the origin coefficients $k_+(t)$, $k_-(t)$, $k_\times(t)$ in (7),(8) when $l=2$:

$$k_+ = -\frac{1}{30}F^{(6)}_{l=2}(t)|_{r=0}, \tag{32a}$$

$$k_- = \frac{1}{10}F^{(6)}_{l=2}(t)|_{r=0}\cos 2\alpha, \tag{32b}$$

$$k_\times = -\frac{1}{10}F^{(6)}_{l=2}(t)|_{r=0}\sin 2\alpha. \tag{32c}$$

For $l>2$ these coefficients are zero.

The $l=2$ solution after rotation corresponds to the following linear combination of waves:

$$\eta = \tilde{\eta}_2(r,t)[-\frac{1}{2}P_{22} + (3-\frac{1}{2}P_{22})\cos 2(\phi-\alpha)], \tag{33a}$$

$$\xi = \tilde{\eta}_2(r,t)3P_{10}\sin 2(\phi-\alpha), \tag{33b}$$

The $l=4$ rotated solution corresponds to the linear combination:

$$\eta = \tilde{\eta}_4(r,t)\{\frac{3}{8}P_{42}+(-\frac{15}{2}+\frac{5}{2}P_{22}+\frac{1}{2}P_{42})\cos 2(\phi-\alpha)+(\frac{5}{2}P_{22}+\frac{1}{8}P_{42})\cos 4(\phi-\alpha)\}, \tag{34a}$$

$$\xi = \tilde{\eta}_4(r,t)\{(-\frac{15}{2}P_{10}+\frac{7}{4}P_{32})\sin 2(\phi-\alpha)+\frac{7}{8}P_{32}\sin 4(\phi-\alpha)\}, \tag{34b}$$

where in the above:

$$\tilde{\eta}_l(r,t) = [c_l + \frac{(a_l - 2f_l)}{l(l+1)}]. \tag{35}$$

.

Expanding F_l near the origin, we find the leading order non-zero terms of $\tilde{\eta}_l$ for $l=2,4$ to be:

$$\tilde{\eta}_2 = -\frac{1}{75}r^2F^{(7)}_{l=2}(t)|_{r=0} \quad (r\to 0), \tag{36}$$

$$\tilde{\eta}_4 = -\frac{1}{79380}r^4F^{(9)}_{l=4}(t)|_{r=0} \quad (r\to 0). \tag{37}$$

This leading order behaviour is consistent with our assumption of cartesian integer expandability near the origin.

The outgoing form for $\tilde{\eta}_l(r,t)$ at asymptotically large radii is:

$$\tilde{\eta}_l(r,t) = \frac{2}{(l-1)l(l+1)(l+2)} r^{-1} F_l^{(l+2)}(t-r) \quad (r \to \infty). \tag{38}$$

Substitution of (38) into (33),(34) gives the outgoing waveform at asymptotically large radii. The transverse traceless amplitudes (to linear order) are then simply:

$$h_+ = -\eta, \tag{39}$$

$$h_\times = \xi. \tag{40}$$

V. The numerically evolved solution

For the $l = 2$ wave test, we choose the wave amplitude function F_l to be:

$$F_{(l=2)}(y) = ay \exp(-y^2). \tag{41}$$

For $l = 4$ we choose:

$$F_{(l=4)}(y) = ay^3 \exp(-y^2), \tag{42}$$

where a is the (small) amplitude of the wave. The extra factor of y^2 in (42) is to simulate more complex radial waveform structure.

The moments $F_l^{(k)}$ in the solutions (26),(27) for our choices (39),(40) for F_l can be automatically generated essentially analytically by repeated application of the recurrence relation:

$$y^p \exp(-y^2) \to (py^{p-1} - 2y^{p+1}) \exp(-y^2), \tag{43}$$

for the mapping on differentiation of the coefficients multiplying the powers of y. Hence if required, the whole linearised solution (for maximal slicing) can be obtained essentially 'analytically' throughout the full spacetime for comparison with numerical code solutions.

An important point to note is that although our 'analytic' solution is for maximal slicing, we can still use it for comparison with the outgoing solution at large radii obtained numerically with mixed slicing. This is because firstly, the choice (41),(42) corresponds at $t = 0$ to time symmetric initial data with (K_1,K_2,K_3,K_+,$K_\times$) all zero. Hence initially the mixed and maximal slicing are equivalent. Secondly during the evolution at large r where we monitor the outgoing wave, h_+,$h_\times$ are gauge invariant while the coordinates times agree (differing only by terms $\sim a^2/r$).

h_+ and $h_\times$ can be spectrally represented (to linear order) in the following manner [1]:

$$h_+ = (-E_{\rm axis} \cos(2\phi) + D_{\rm axis} \sin(2\phi))$$

$$- \sum_{l=2,4,6\ldots} (a_l + a_{l0}\cos(2\phi) + b_{l0}\sin(2\phi))P_{l2}$$

$$- \sum_{\substack{l=2,4,6,\ldots \\ m=2,4,\ldots,l}} (a_{lm}\cos((m+2)\phi) + b_{lm}\sin((m+2)\phi))P_{lm}, \qquad (44a)$$

$$h_\times = (D_{\rm axis}\cos(2\phi) + E_{\rm axis}\sin(2\phi))P_1$$

$$+ \sum_{l=3,5,7\ldots} (a'_l + a'_{l0}\cos(2\phi) + b'_{l0}\sin(2\phi))P_{l2}$$

$$+ \sum_{\substack{l=3,5,7\ldots \\ m=2,4,..,l-1}} (a'_{lm}\cos((m+2)\phi) + b'_{lm}\sin((m+2)\phi))P_{lm}, \qquad (44b)$$

where the spectral amplitudes $D_{\rm axis}$,$E_{\rm axis}$; a_l; a_{l0},b_{l0}; a_{lm},b_{lm} and their primed counterparts, are functions of radius and time. These expansions are used to spectrally resolve the angular dependence of the numerically obtained outgoing waves on the angular grid points at each radius.

For the numerical evolution, we have used an outer grid radius of 10 units; a grid of (100x11x16) (r,θ,ϕ) grid points; and an amplitude $a = 10^{-5}$ for $l = 2$ and $a = 10^{-8}$ for $l = 4$. r_0 is 1.4534 units, and $n = 2.5$ (see eq.(6)). We have taken $\alpha = 0$. (Details of the numerical code will be given in a separate paper [9]). The expected non-zero asymptotic amplitudes (for these values) are, for $l = 2$:

$$[E_{\rm axis}, a_2, a_{20}] = \frac{1}{24}\,[6,-1,-1]\; r^{-1}F^{(4)}_{(l=2)}(t-r) \quad (r\to\infty), \qquad (45a)$$

where:

$$F^{(4)}_{(l=2)}(y) = a\exp(-y^2)(60y - 80y^3 + 16y^5), \qquad (45b)$$

while for $l = 4$:

$$[E_{\rm axis}, a_4, a_{20}, a_{40}, a_{22}, a_{42}, b'_{30}, b'_{32}] = \frac{1}{1440}\,[-60,3,20,4,20,1,14,7]$$
$$r^{-1}F^{(6)}_{(l=4)}(t-r) \quad (r\to\infty) \qquad (46a)$$

with:

$$F^{(6)}_{(l=4)}(y) = a\exp(-y^2)(2520y - 7560y^3 + 5040y^5 - 1056y^7 + 64y^9). \qquad (46b)$$

Figures 1-11 show a comparison of the numerically computed non-zero spectral outgoing amplitudes versus the theoretically expected asymptotic waveform amplitudes (45),(46). Figures 1-3 show results for the $l = 2$ test; figures 4-11 results for the $l = 4$ test. The numerical waveforms are measured at the outer grid radius of 10 units. Reasonable agreement is obtained, although the later part of the numerical waveforms tend to damp too slowly and eventually show irregularity. The present preliminary setup of our code is unable to run much further than shown because of stability difficulties. Further work is currently underway to overcome these problems.

The tests presented here are derived from rotated axisymmetry solutions, and are not the most general non-axisymmetric test possible. More generally, radial gauge coordinates satisfying the origin regularity conditions will not have all metric and shift variables which explicitly fall-off asymptotically at large radii [1]. These more general types of tests will be dealt with in a separate paper [9].

Acknowledgements

A grant under the International Centre for Theoretical Physics (ICTP)/Slovenia cooperation program sponsored by the Slovenian Ministry of Science is gratefully acknowledged (R.F.S.). One of us (R.F.S.) is especially grateful to Prof. Andrej Cadez for his keen interest, encouragement and support. This work has also been supported by an EEC fellowship (R.F.S.) at the Scuola Internazionale Superiore di Studi Avanzati (SISSA) within the Human Capital and Mobility research programme. We are especially grateful to Prof. Dennis Sciama for the support of this fellowship, as well as additional SISSA and ICTP fellowship support. One of us (R.F.S.) thanks Drs. John Miller and Antonio Lanza for their interest. We also thank Alvise Nobile, Head of the Computer Center of the ICTP, and his staff for their assistance. Use of the ICTP computational facilities, as well as those at the Department of Physics, University of Ljubljana are acknowledged.

References:

1. L. Sigalotti and R.F. Stark, Non-axisymmetric rotating gravitational collapse and gravitational radiation: theoretical background, to be submitted to *Phys.Rev.*D..

2. R.F. Stark, 1989, in *Frontiers in numerical relativity*, Eds. C.R.Evans, L.S.Finn & D.W.Hobill, (Cambridge University Press).

3. D.M. Eardley, 1980, Unpublished working notes.

4. J.M. Bardeen and T. Piran, 1983, *Physics Reports*, **96**, 205.

5. J.M. Bardeen, 1983, unpublished private communication.

6. J.M. Bardeen, 1983, in *Gravitational Radiation*, eds. N.Deruelle and T.Piran, (North-Holland, Amsterdam).

7. R.F. Stark and T. Piran, 1987, *Computer Physics Reports*, **5**, 221.

8. S.A. Teukolsky, 1982, *Phys.Rev.*D., **26**, 745.

9. L. Sigalotti and R.F. Stark, Non-axisymmetric rotating gravitational collapse and gravitational radiation: numerical methods and tests, in preparation.

Figure captions:

Fig.1: $l = 2$ wave test; $E_{\rm axis}$ amplitude (see eqs.(44),(45)) vs. retarded time $(t-r)$; numerical and theoretical curves. Comparison of the measured outgoing amplitude (full curve) from the full numerical code with the theoretical linearised prediction (broken curve). The amplitude is normalised by the small initial amplitude a. Show is the variation of the amplitude vs. retarded time. The numerical solution is obtained at the outer grid radius of 10 units. The theoretical curve is that for asymptotically large radii.

Fig.2: $l = 2$ wave test; a_2 amplitude (see eqs.(44),(45)) vs. retarded time $(t-r)$; numerical and theoretical curves. (see also Fig.1 caption).

Fig.3: $l = 2$ wave test; a_{20} amplitude (see eqs.(44),(45)) vs. retarded time $(t-r)$; numerical and theoretical curves. (see also Fig.1 caption).

Fig.4: $l = 4$ wave test; $E_{\rm axis}$ amplitude (see eqs.(44),(46)) vs. retarded time $(t-r)$; numerical and theoretical curves. (see also Fig.1 caption).

Fig.5: $l = 4$ wave test; a_4 amplitude (see eqs.(44),(46)) vs. retarded time $(t-r)$; numerical and theoretical curves. (see also Fig.1 caption).

Fig.6: $l = 4$ wave test; a_{20} amplitude (see eqs.(44),(46)) vs. retarded time $(t-r)$; numerical and theoretical curves. (see also Fig.1 caption).

Fig.7: $l = 4$ wave test; a_{40} amplitude (see eqs.(44),(46)) vs. retarded time $(t-r)$; numerical and theoretical curves. (see also Fig.1 caption).

Fig.8: $l = 4$ wave test; a_{22} amplitude (see eqs.(44),(46)) vs. retarded time $(t-r)$; numerical and theoretical curves. (see also Fig.1 caption).

Fig.9: $l = 4$ wave test; a_{42} amplitude (see eqs.(44),(46)) vs. retarded time $(t-r)$; numerical and theoretical curves. (see also Fig.1 caption).

Fig.10: $l = 4$ wave test; b'_{30} amplitude (see eqs.(44),(46)) vs. retarded time $(t-r)$; numerical and theoretical curves. (see also Fig.1 caption).

Fig.11: $l = 4$ wave test; b'_{32} amplitude (see eqs.(44),(46)) vs. retarded time $(t-r)$; numerical and theoretical curves. (see also Fig.1 caption).

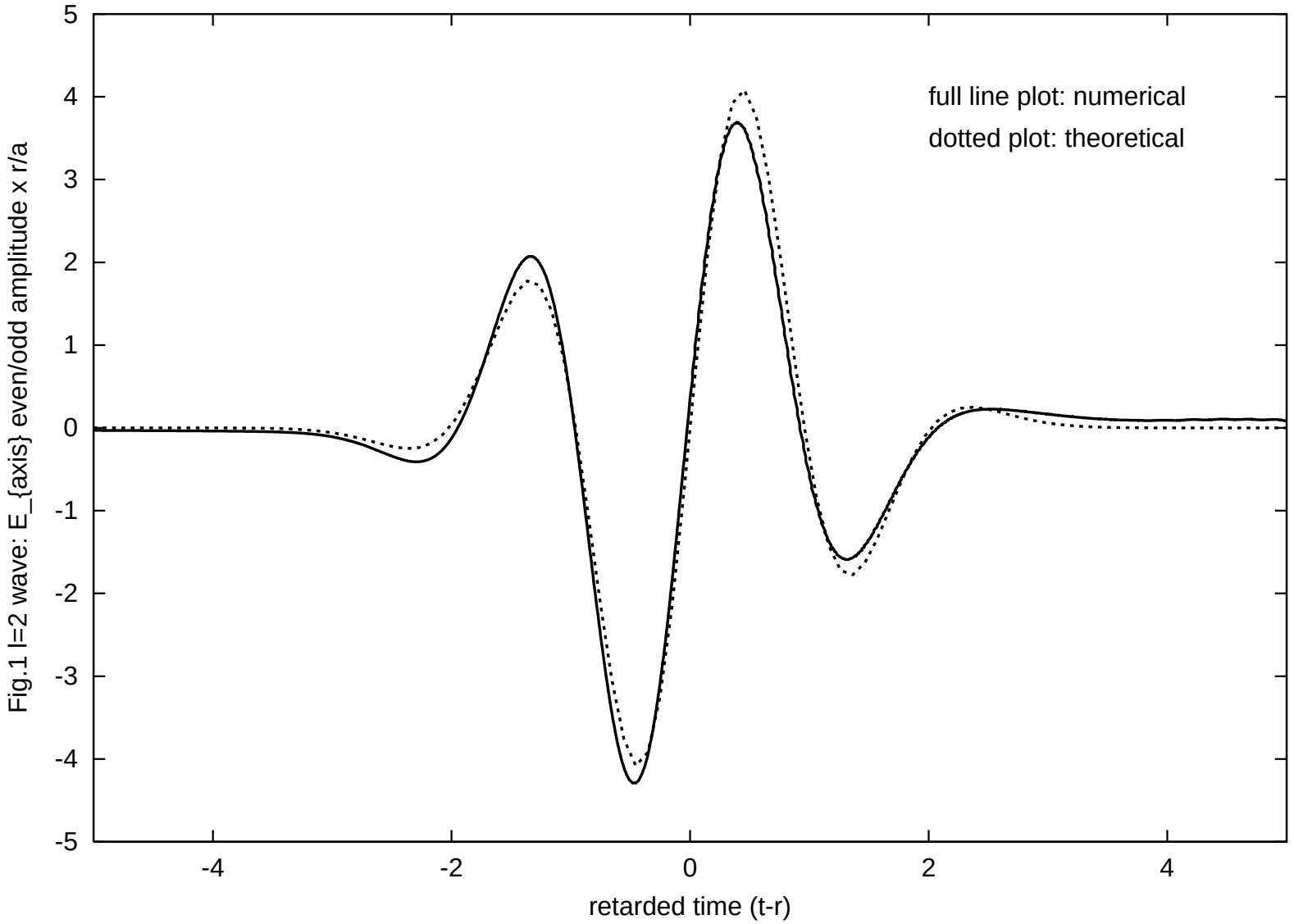
full line plot: numerical
dotted plot: theoretical
Fig.1 l=2 wave: E_{axis} even/odd amplitude x r/a
retarded time (t-r)
5
4
3
2
1
0
-1
-2
-3
-4
-5
-4
-2
0
2
4

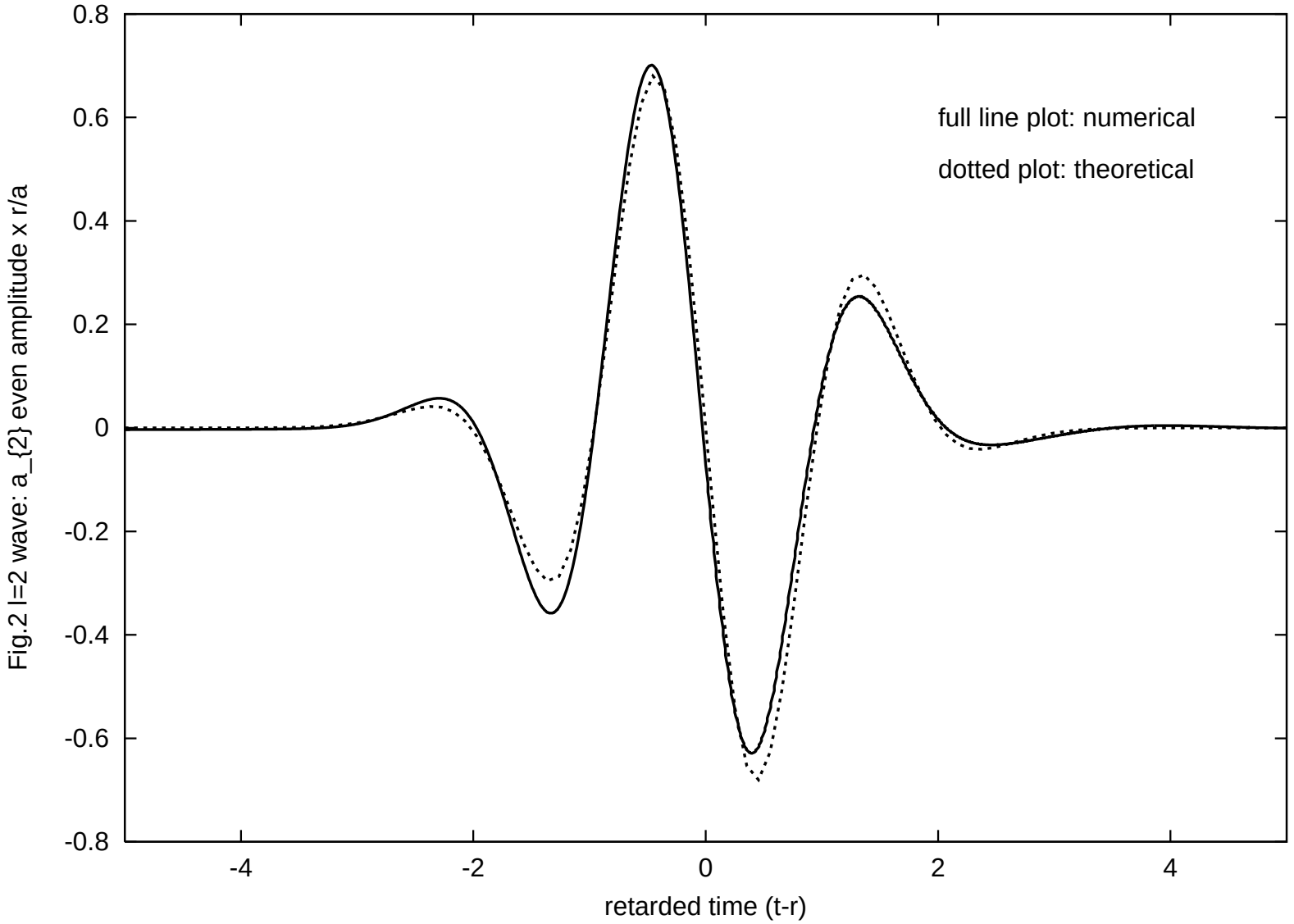
0.8
0.6
0.4
0.2
0
-0.2
-0.4
-0.6
-0.8
-4
-2
0
2
4
retarded time (t-r)
full line plot: numerical
dotted plot: theoretical
Fig.2 l=2 wave: a_{2} even amplitude x r/a

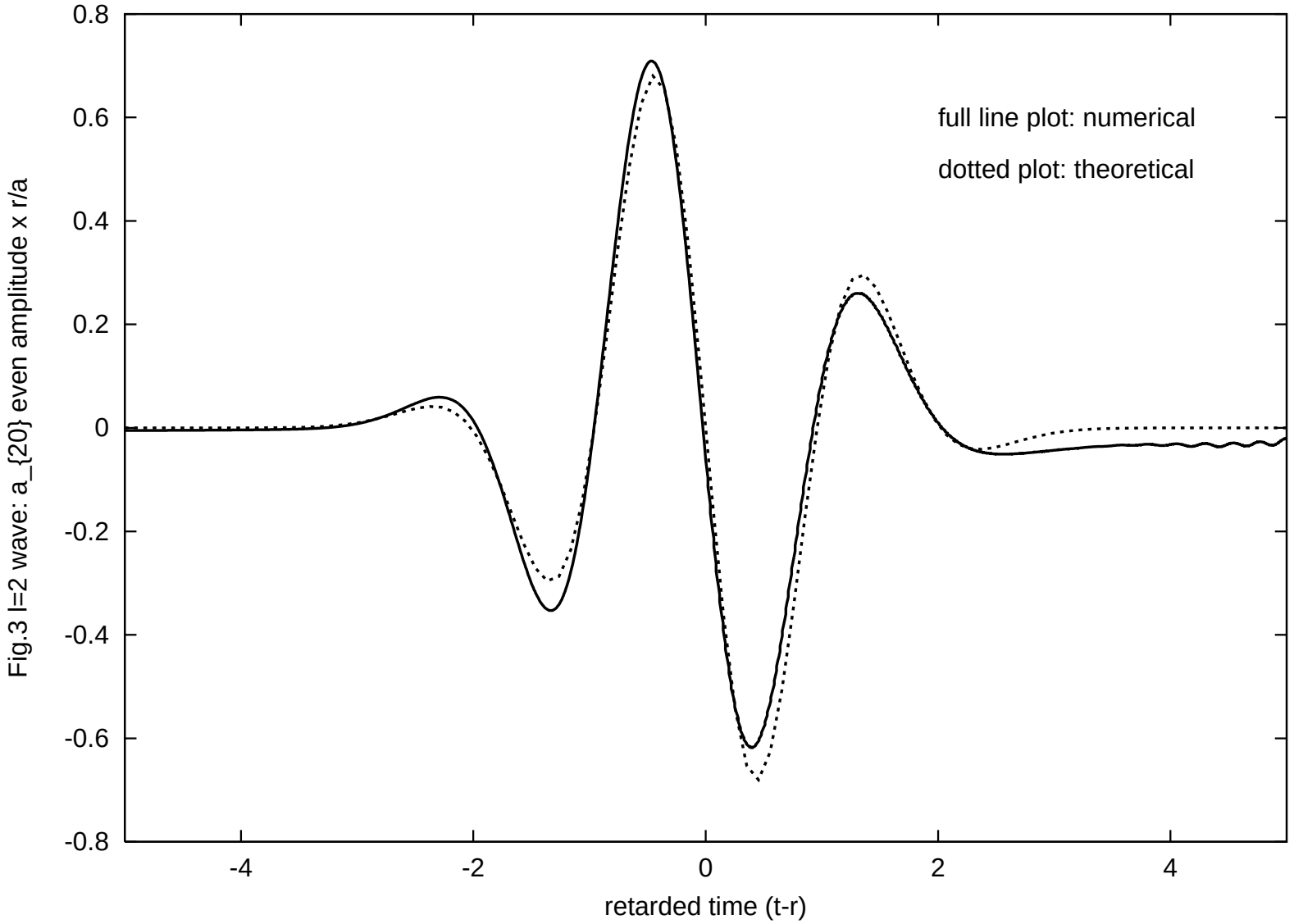
0.8
0.6
0.4
0.2
0
-0.2
-0.4
-0.6
-0.8
-4
-2
0
2
4
retarded time (t-r)
Fig.3 l=2 wave: a_{20} even amplitude x r/a
full line plot: numerical
dotted plot: theoretical

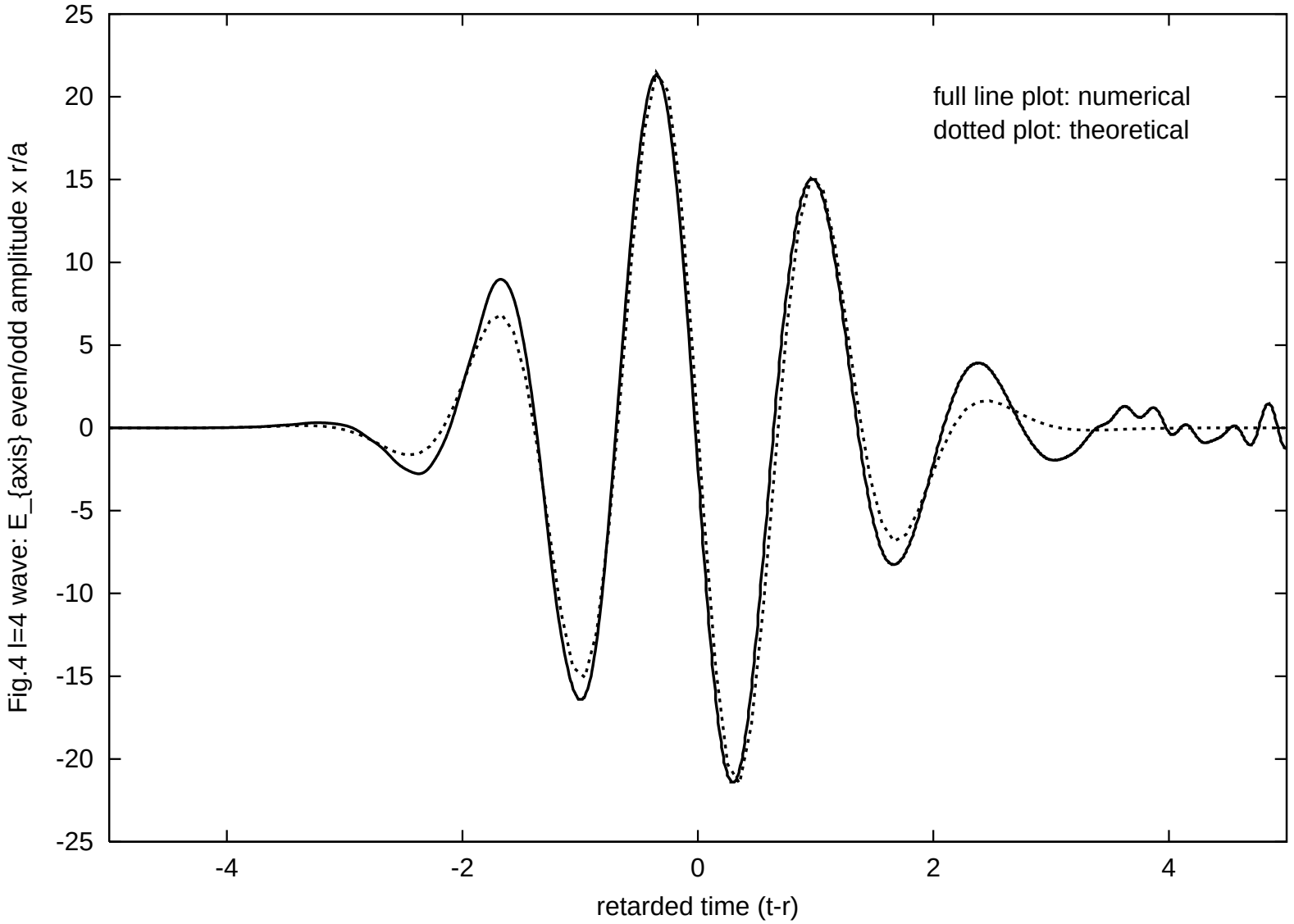
full line plot: numerical
dotted plot: theoretical
Fig.4 l=4 wave: E_{axis} even/odd amplitude x r/a
retarded time (t-r)
25
20
15
10
5
0
-5
-10
-15
-20
-25
-4
-2
0
2
4

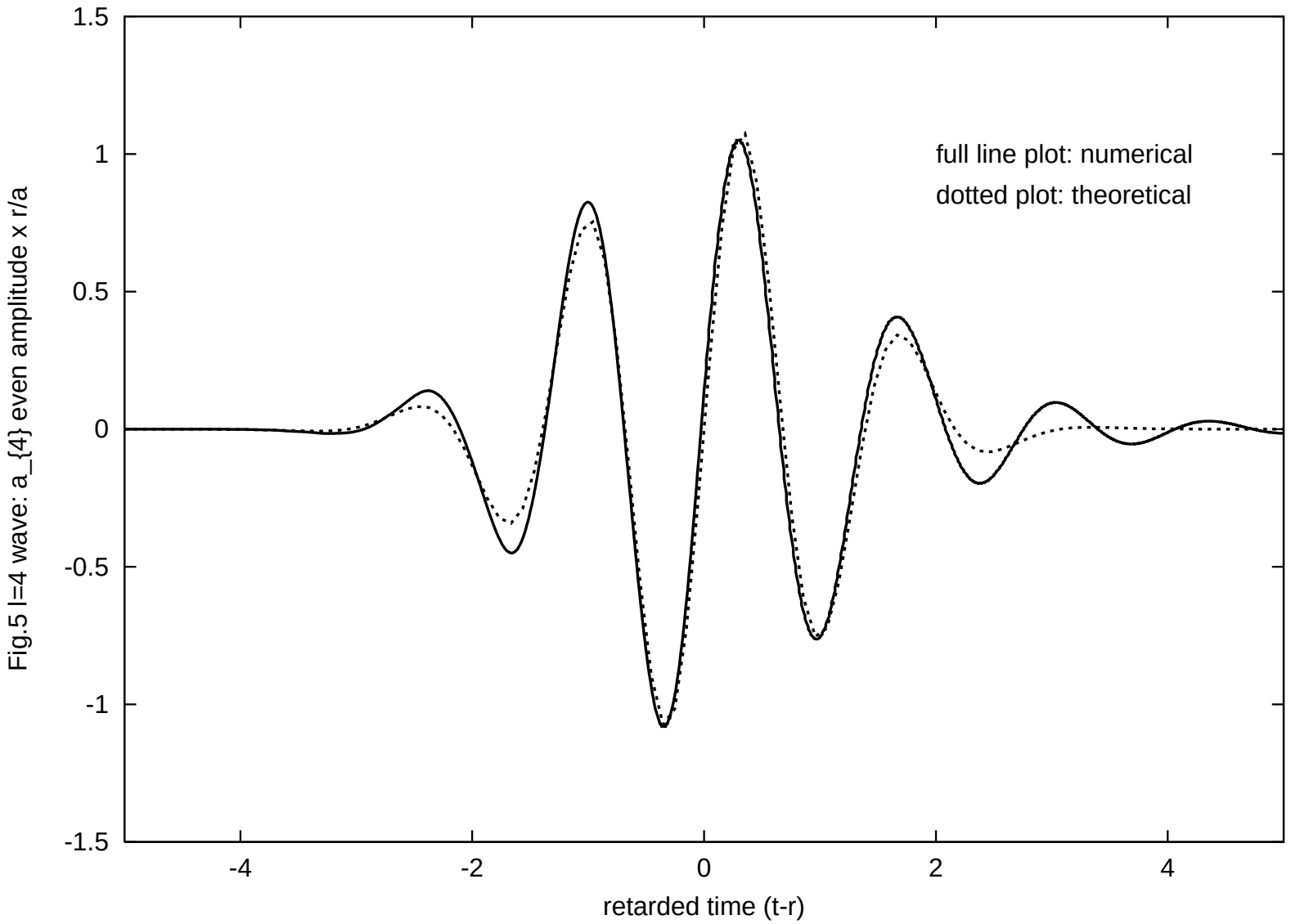

Fig.5 l=4 wave: a_{4} even amplitude x r/a

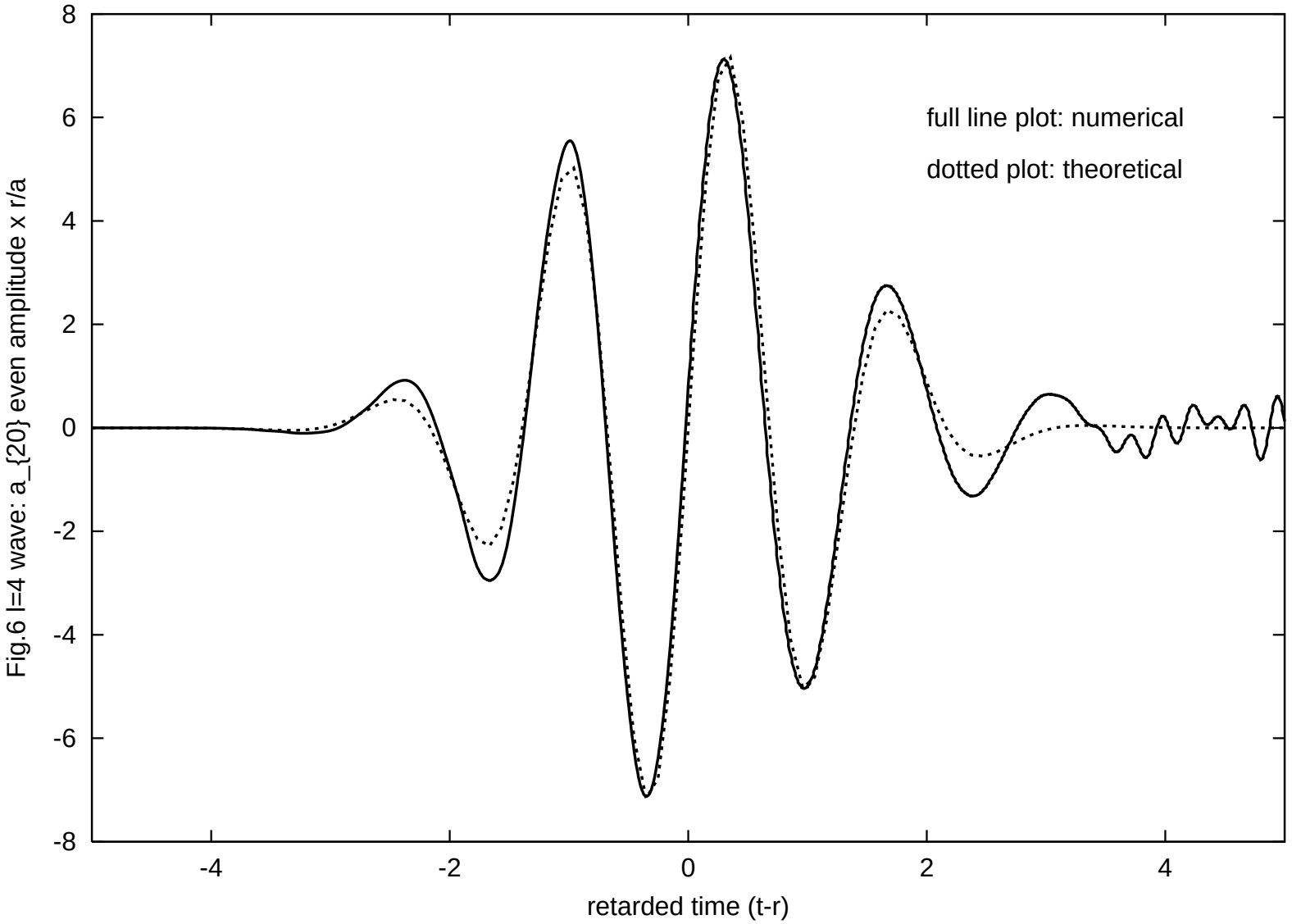
full line plot: numerical
dotted plot: theoretical
Fig.6 l=4 wave: a_{20} even amplitude x r/a
retarded time (t-r)
8
6
4
2
0
-2
-4
-6
-8
-4
-2
0
2
4

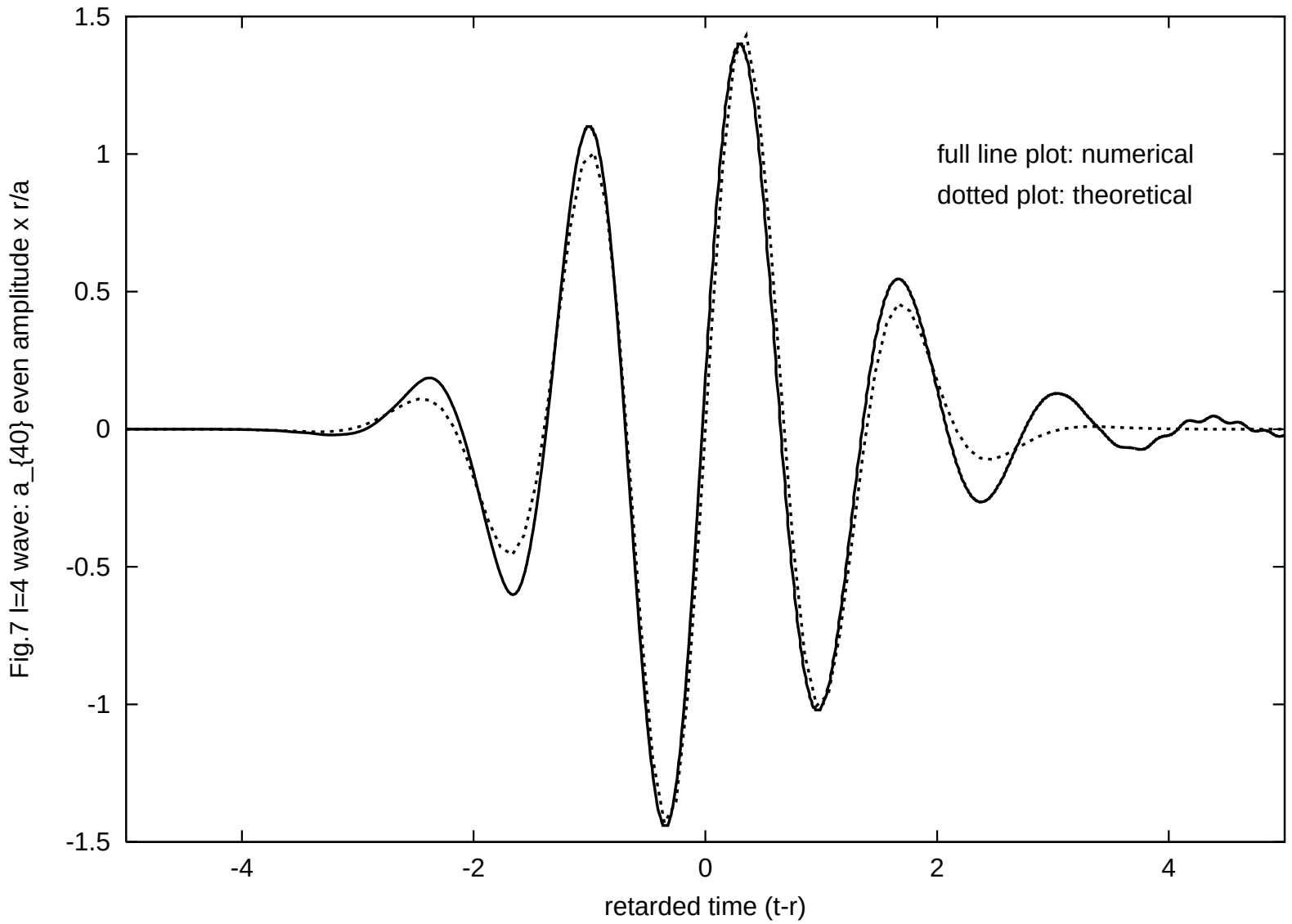
1.5
1
0.5
0
-0.5
-1
-1.5
-4
-2
0
2
4
retarded time (t-r)
Fig.7 l=4 wave: a_{40} even amplitude x r/a
full line plot: numerical
dotted plot: theoretical

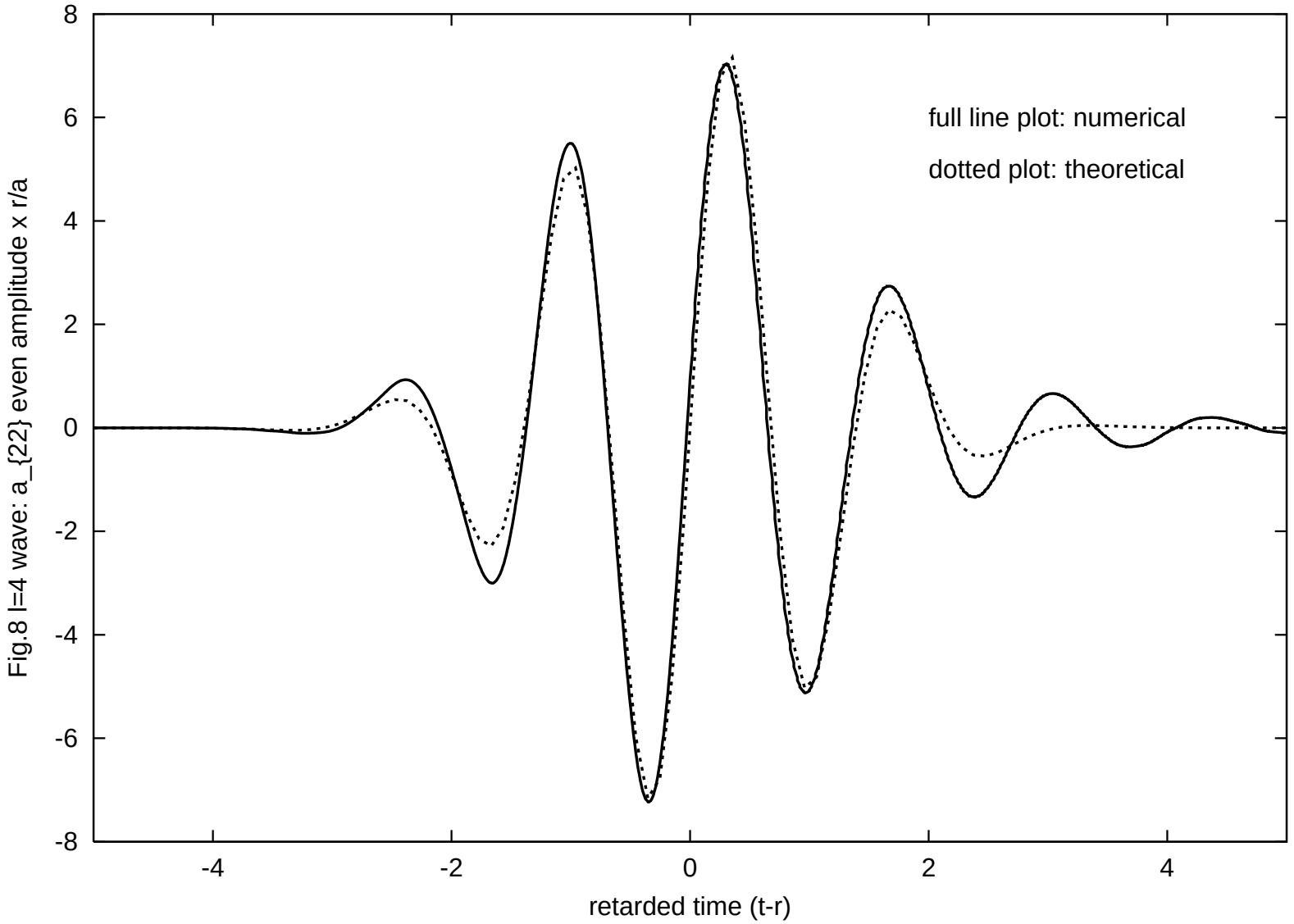
full line plot: numerical
dotted plot: theoretical
Fig.8 l=4 wave: a_{22} even amplitude x r/a
retarded time (t-r)
8
6
4
2
0
-2
-4
-6
-8
-4
-2
0
2
4

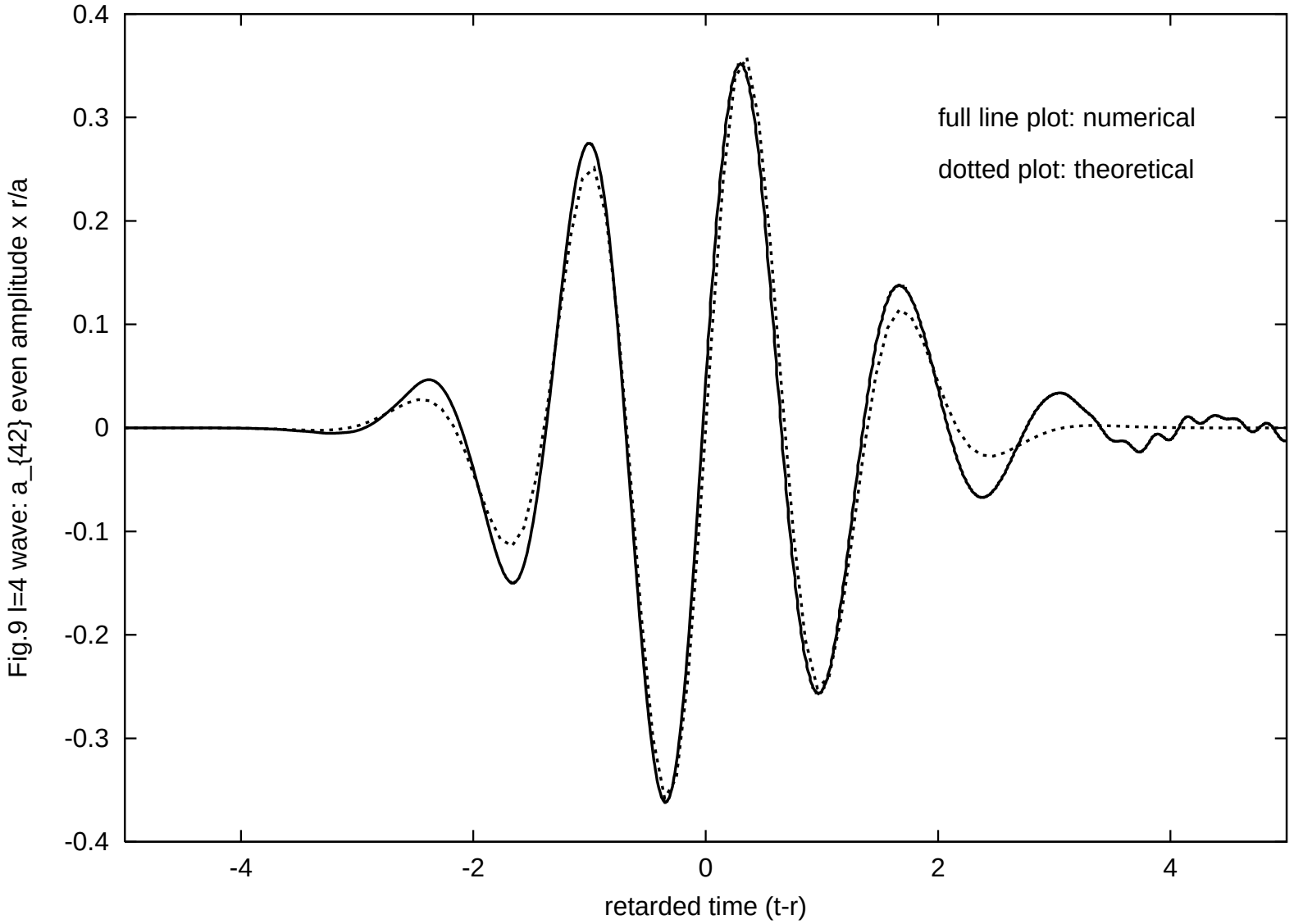
0.4
0.3
0.2
0.1
0
-0.1
-0.2
-0.3
-0.4
-4
-2
0
2
4
retarded time (t-r)
full line plot: numerical
dotted plot: theoretical
Fig.9 l=4 wave: a_{42} even amplitude x r/a

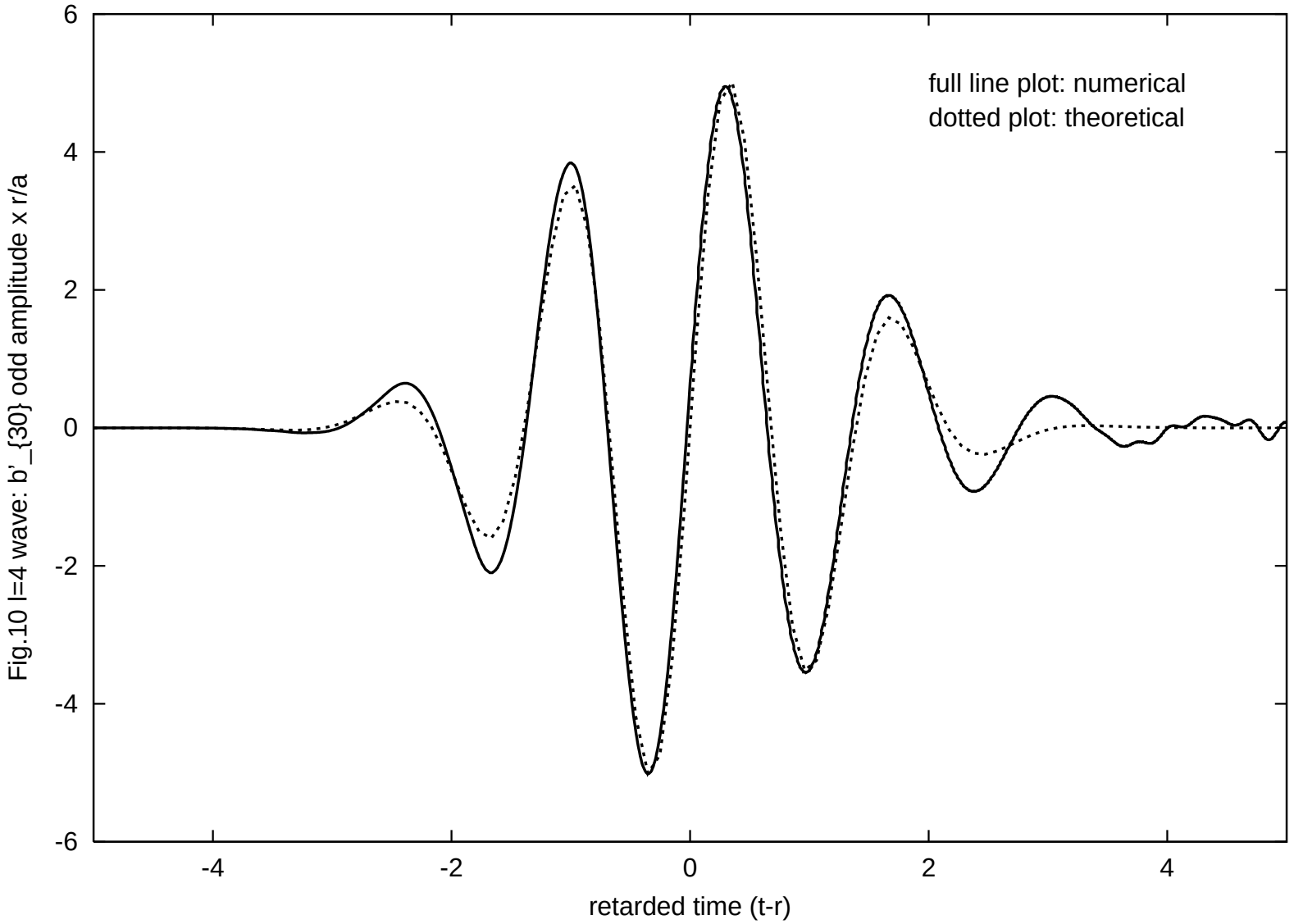
full line plot: numerical
dotted plot: theoretical
Fig.10 l=4 wave: b'_{30} odd amplitude x r/a
retarded time (t-r)
6
4
2
0
-2
-4
-6
-4
-2
0
2
4

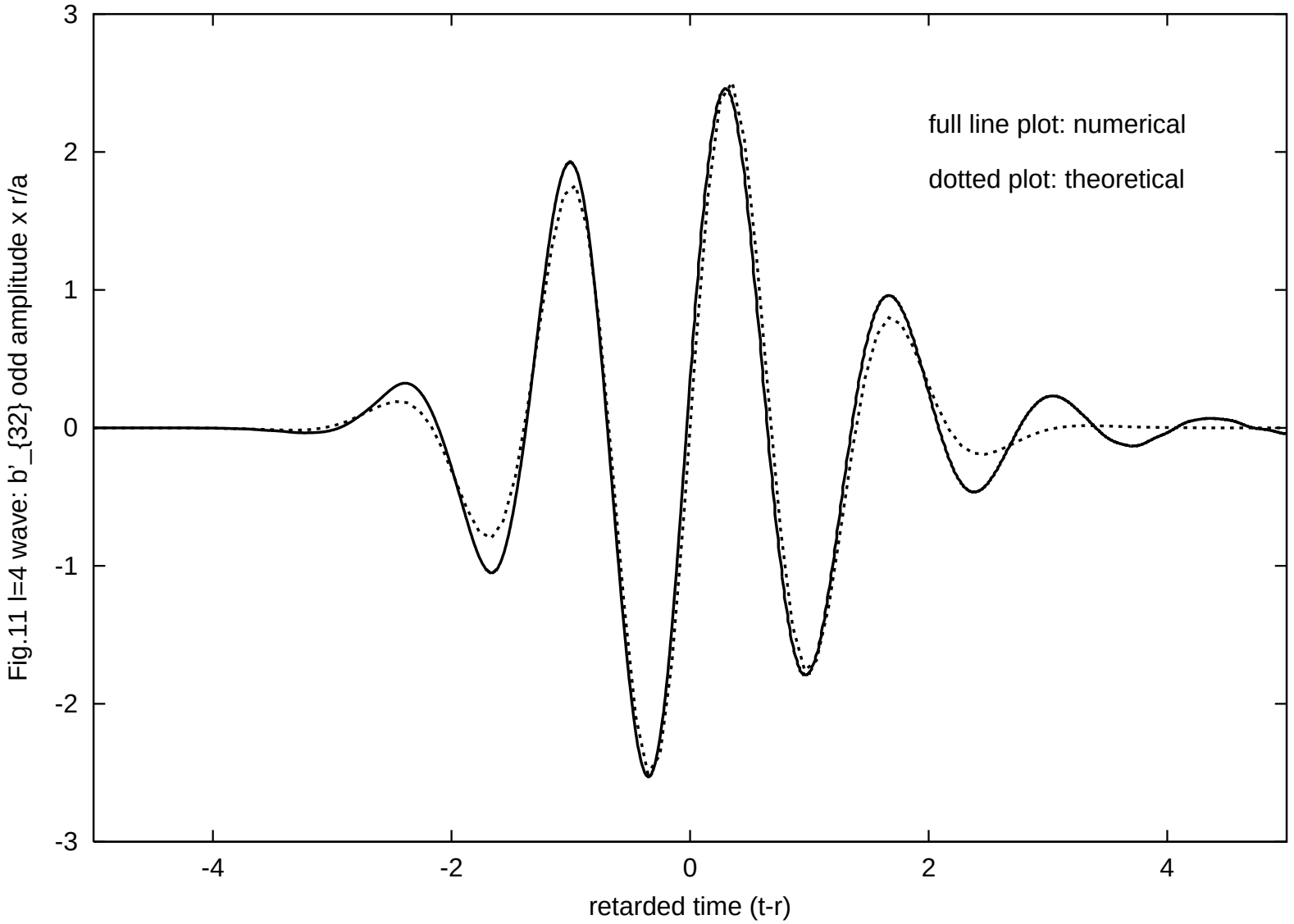
full line plot: numerical
dotted plot: theoretical
Fig.11 l=4 wave: b'_{32} odd amplitude x r/a
retarded time (t-r)
3
2
1
0
-1
-2
-3
-4
-2
0
2
4